Supplementary Information for

A Metamaterial Scaffold Beyond Modulus Limits: Enhanced Osteogenesis and Angiogenesis of Critical Bone Defects

Yu Qin[1, 2, 5], Zehao Jing[2, 5], Da Zou[2], Youhao Wang[2], Hongtao Yang[3], Kai Chen[1], Weishi Li[2*], Peng Wen[4*], Yufeng Zheng[1*]

* Corresponding authors: Weishi Li (puh3liweishi@163.com), Peng Wen (wenpeng@tsinghua.edu.cn), Yufeng Zheng (yfzheng@pku.edu.cn)

Contents

Supplementary Note 1: Design and compression test

The designed porosity of CS, CS2 and TMS is 77.8%, 78.8% and 78.5 %, respectively. And the as-built porosity of CS, CS2 and TMS calculated from micro-CT is 73.3±0.3 % 74.1±0.5 % and 73.1±0.2 %, respectively. As illustrated in Fig. S2, all springs are constructed from squares through a rotary scan process. Taking the outer ring as an example, the four springs (No.1, 2, 3, and 4) are divided into two groups: one group is marked with blue squares (No.1 and No.2), while the other group is marked with yellow squares (No.3 and No.4). When pillars are added to connect each group, the small gap (lg) of the TMS structure is formed.

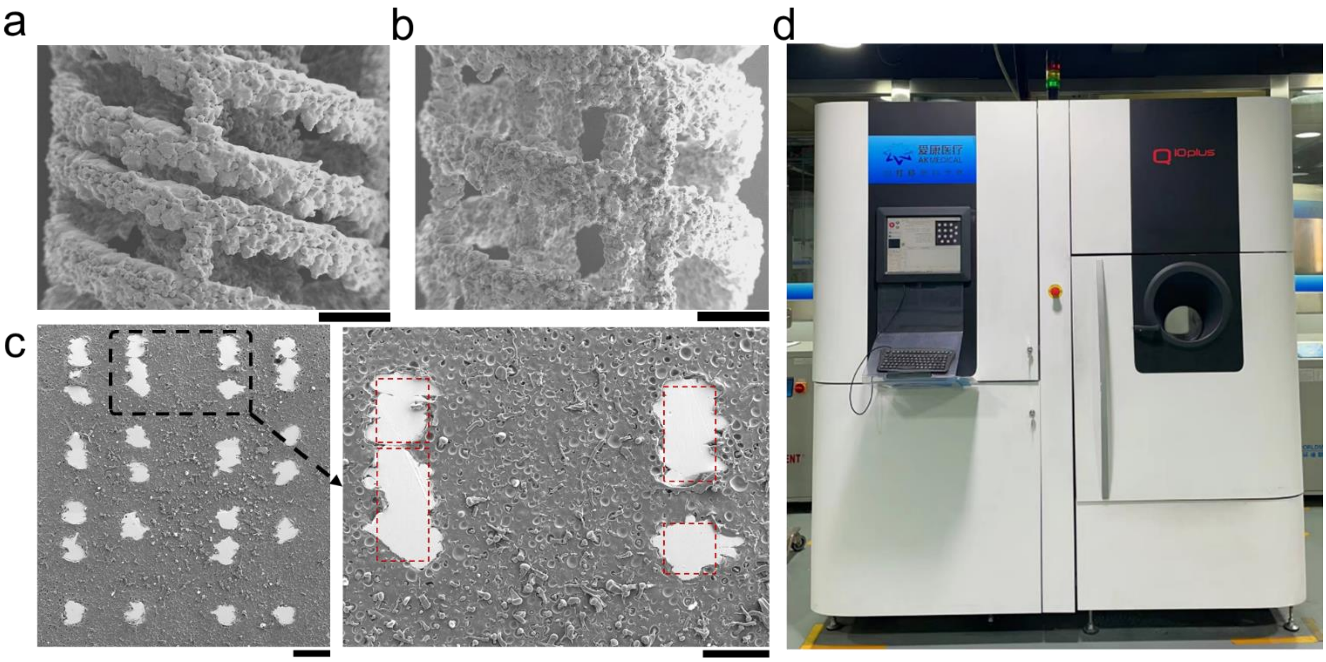

Fig. S1 3D printed scaffolds. a and b, SEM pictures of as-built TMS and CS scaffolds, respectively. Scale bars = 1 mm **c** Cross-sectional view of as- built TMS compared with designed structure (dashed box). scale bar = 1 mm and 500 μm, respectively. **d** EBPBF machine

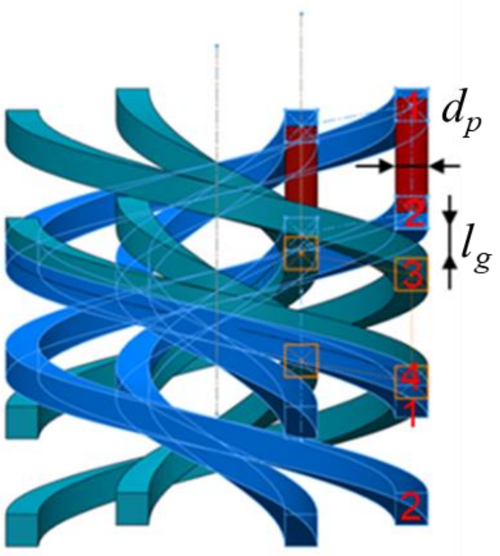

Fig. S2 Establishment of TMS springs and pillars. 4 springs are contained in the exterior of TMS with numbers from 1 to 4. Pillars is added in the middle of spring 1, 2 and spring 3, 4.

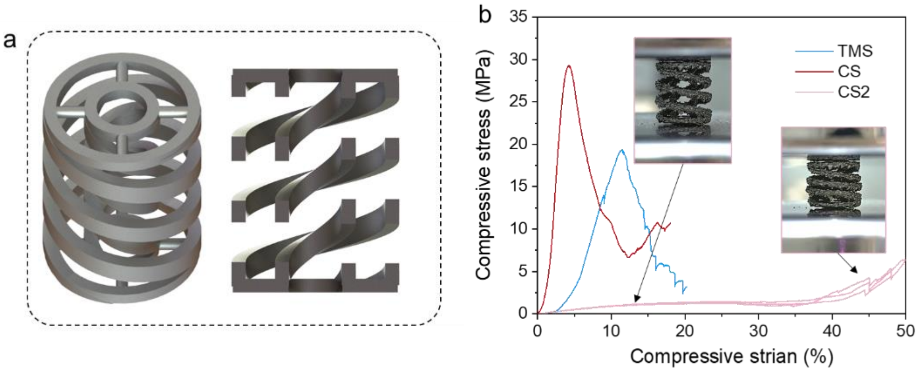

Fig. S3 Design and compression properties of CS2. (a) Three-dimensional design and sagittal cross-section of CS2 (b) Compression strain-stress curves of CS2 compared with CS and TMS

Supplementary Note 2: Three-point bending properties

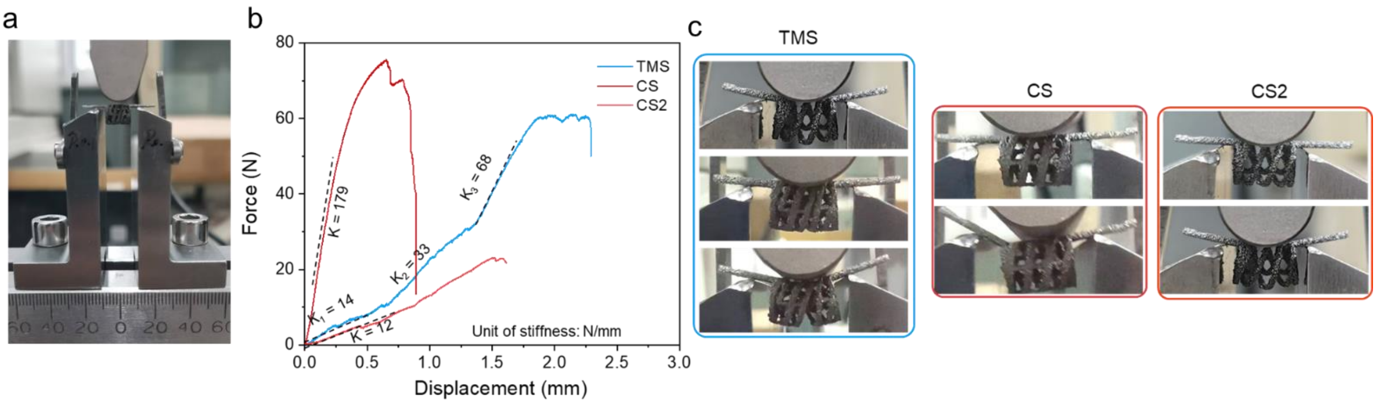

Fig. S4 Three-point bending tests of TMS, CS and CS2. a Experiment setup with a span length of 10 mm. **b** Displacement-force curves. The bending stiffness k were calculated using segmental force divided by displacement**. c** Different bending stages of tested samples

Supplementary Note 3: Effects of design parameters to mechanical behaviors

To analyzes the design parameters' effect on strain-stress curve, we conducted numerical simulations as shown in Fig. S5. It can be found that by increasing l_g, the spacing between the two springs is enlarged (Fig. S5a). And t the strain required for the TMS to complete the first stage is then increased. Meanwhile, changing l_g does not change the pitch and thickness of the springs, so its stiffness can be kept constant in the first stage according to Hooke's law. Similarly, increasing only the diameter of the pillars does not affect the stiffness in the first stage, as shown in Fig.S5b. But the stress is significantly higher for increased pillars at the second stage. Further increase of only the side length of the spring enhances the modulus of the first stage, while the second stage remains almost unchanged. Since the modulus of the spring is so much smaller than the modulus of the pillars, the modulus of the second stage is almost equal to the modulus of the pillar, thus remain intact.

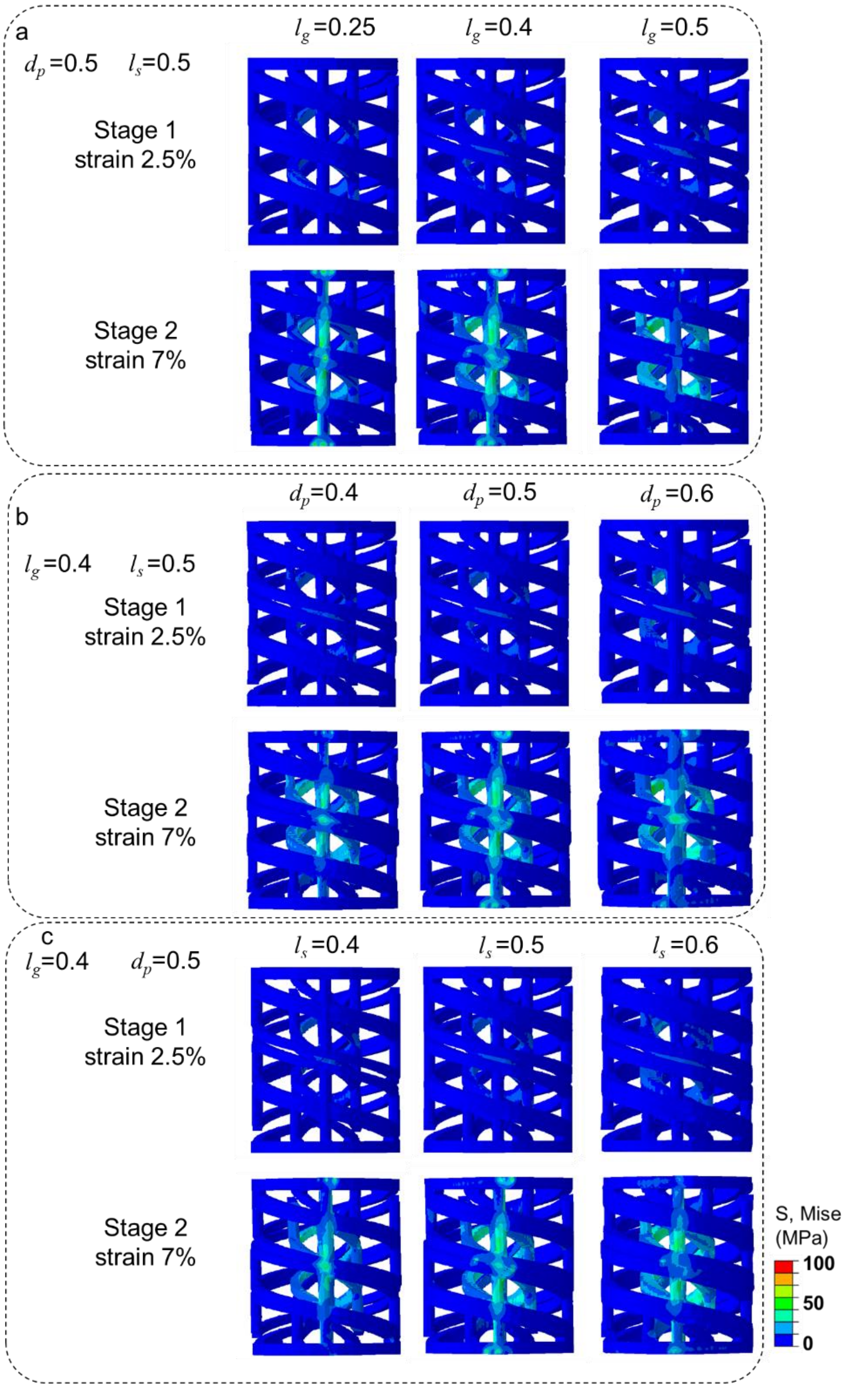

Fig. S5 Effect of design parameters on von-Mise stress under different strain by FEM. a l_g. b d_p. **c** l_s.

Supplementary Note 4: Fatigue properties

The fatigue ratcheting and fatigue damage strain were calculated from the displacement data (Fig. S6a) according to reference [1]. The fatigue ratcheting strain was defined as the translation of the minimum strain of each hysteresis loop from the 100th cycle, where the loading stress became stable. While the fatigue damage strain was defined as the difference of the hysteresis loop strains between the current and the 100th cycles.

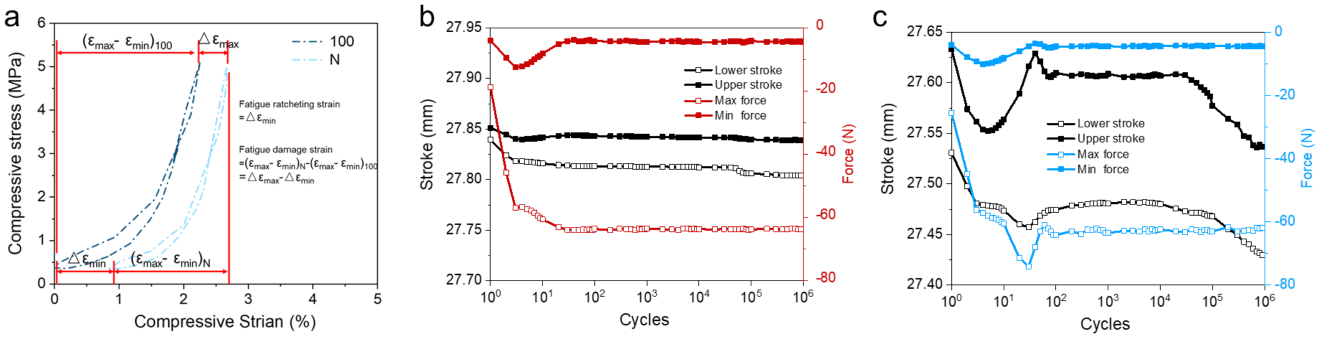

Fig. S6 Compression fatigue properties of CS and TMS. a, b hysteresis loops for CS and TMS shift along the strain axis. **c, d** Force and load indenter position curves. **e, f** Calculation of fatigue ratcheting and fatigue damage strains.

Supplementary Note 5: Surgery procedure

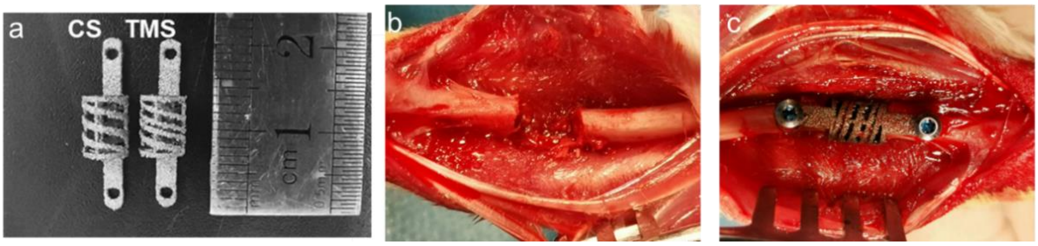

Fig. S7 Surgery procedure of critical bone defects. a Plates for screw fixation were incorporated with the scaffolds for CS and TMS. **b** surgery modelling of critical bone decfects. **c** Ulnas implanted with TMS.

Supplementary Note 6: Radiographic follow-up images

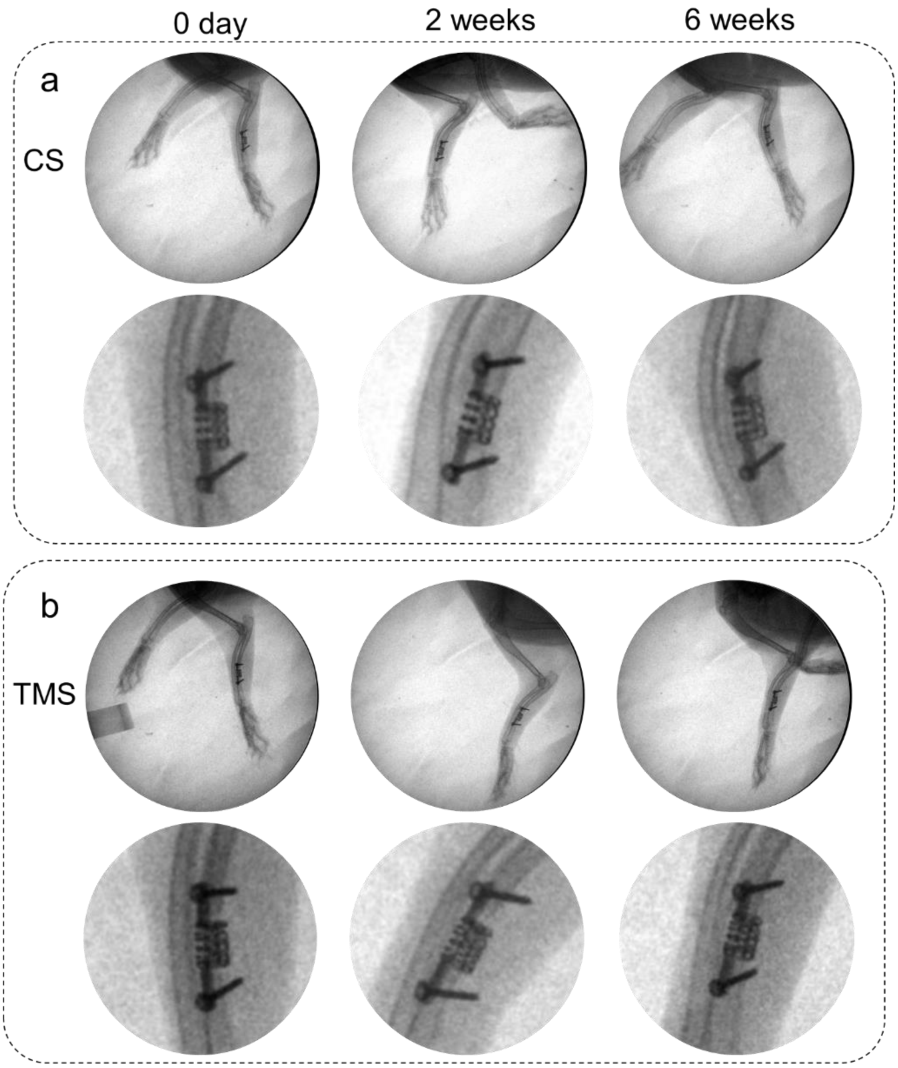

Fig S8 X-ray images of implanted CS and TMS in rabbits' ulnar defects at 0, 2 and 6 weeks. a CS. **b** TMS.

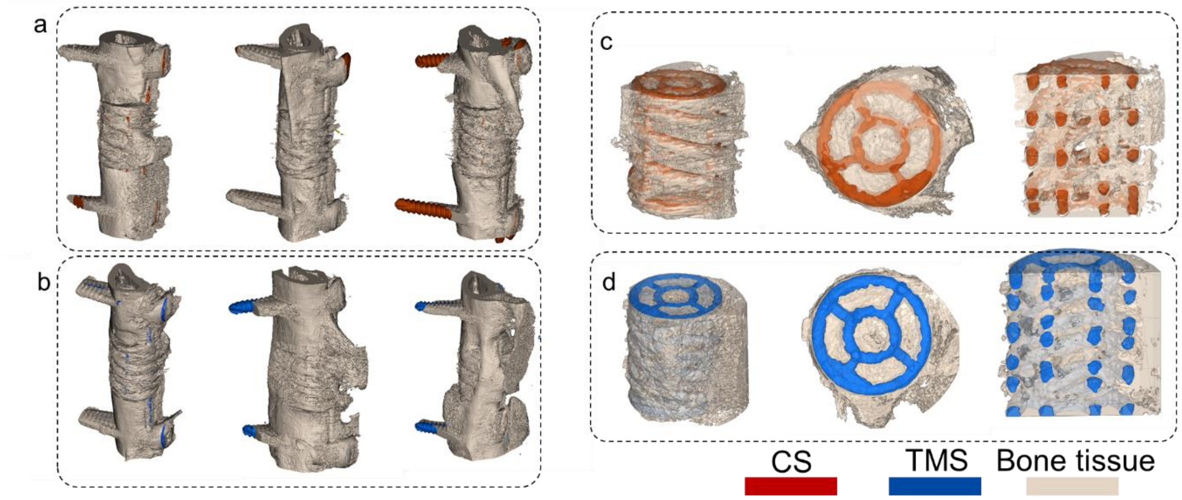

Fig. S9 3D reconstruction from micro-CT scanning at 4 weeks. a, b CS and TMS with three replicates. **c, d** ROI reconstruction with top and cross-sectional views.

Supplementary Note 7: Bone reconstruction of CS2

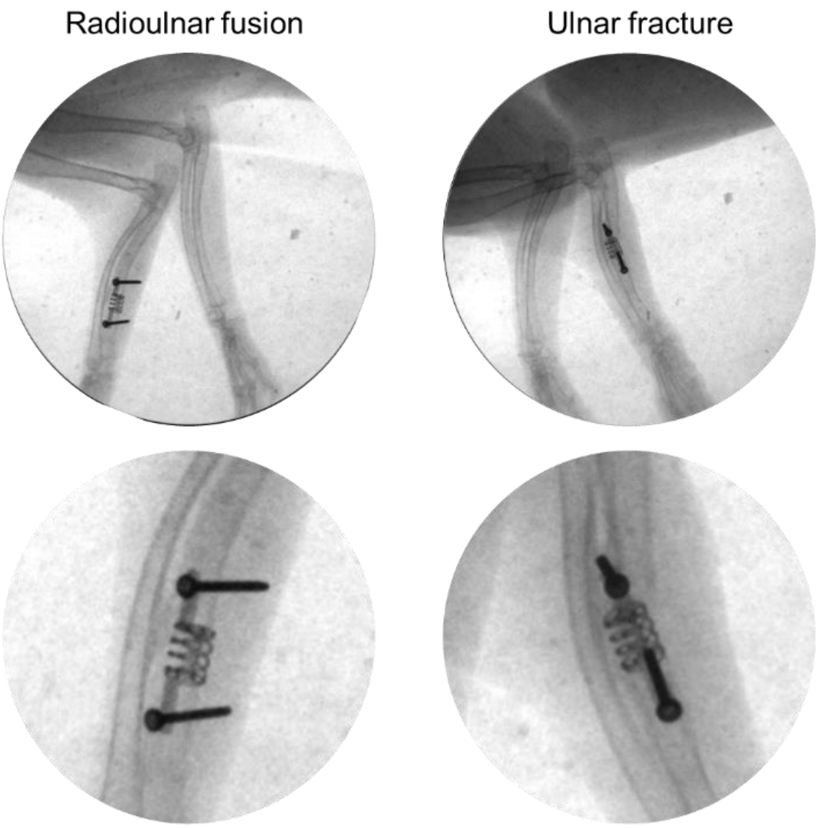

Fig. S10 X-ray images of CS2 at 4 weeks post-implantation. Left column shows radioulnar fusion defects and its magnificent observation. Right column shows fracture defects and its magnificent observation.

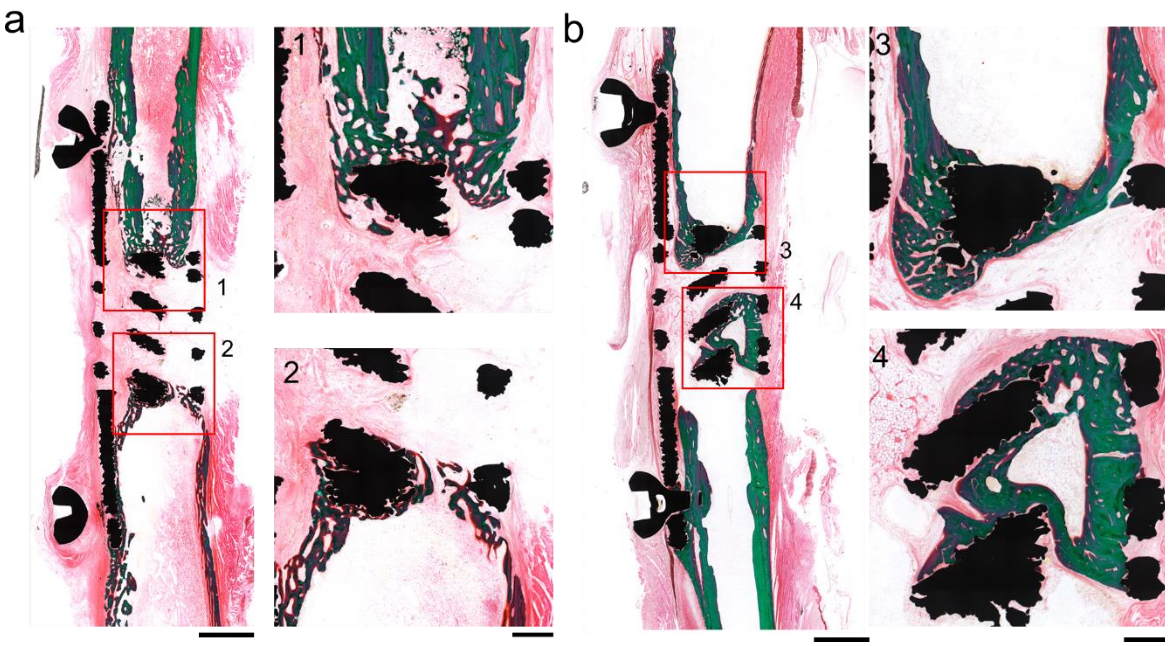

Fig. S11 Histomorphological evaluations of CS2. a 4 weeks with scale bar = 3 mm and enlarged pictures of two areas with scale bar = 500 µm**. b** 8 weeks with scale bar = 3 mm and enlarged pictures of two areas with scale bar = 500 µm

Supplementary Note 8: Mirostructure of bone reconstruction

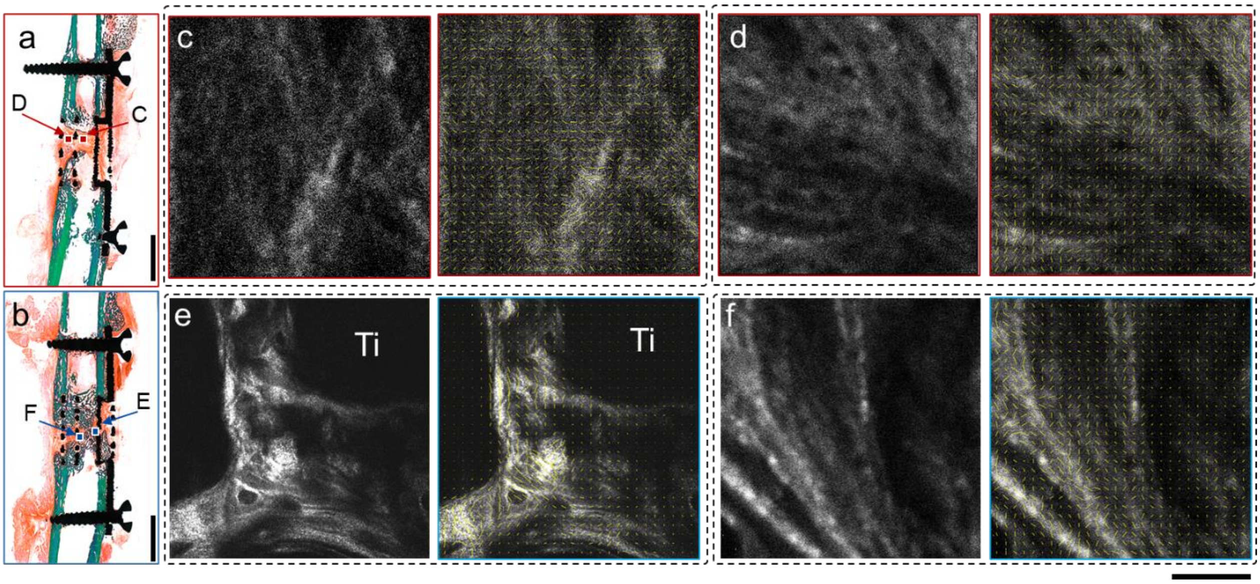

Fig. S12 SHG imaging of fiber orientation of bone tissues. a,b position of tested fiber orientation with implantation of CS and TMS. **c-d** Magnifications of label ROI with SHG imaging. The primary fiber orientation was visualized as a yellow line in each sub-ROI. The length of the line indicates the degree of anisotropy. Scale bars = 100 µm.

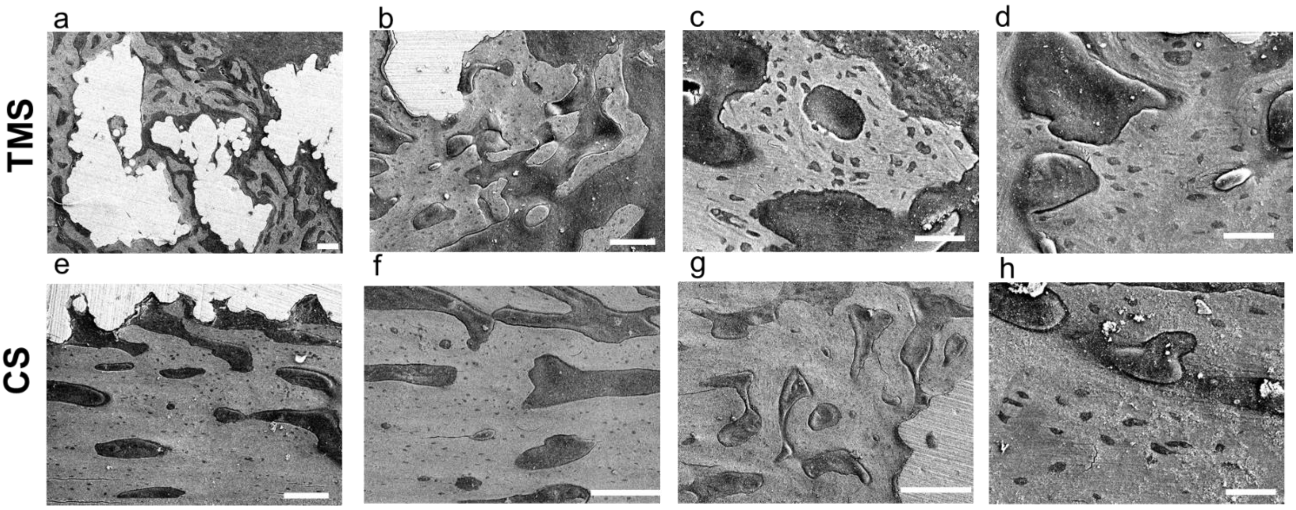

Fig. S13 SEM images of new bone microstructures with scaffolds. **a-d** TMS. **e-h** CS. Scale bars of **a, b, e, f, g** = 100 µm. Scale bars of **c, d, h** = 20 µm

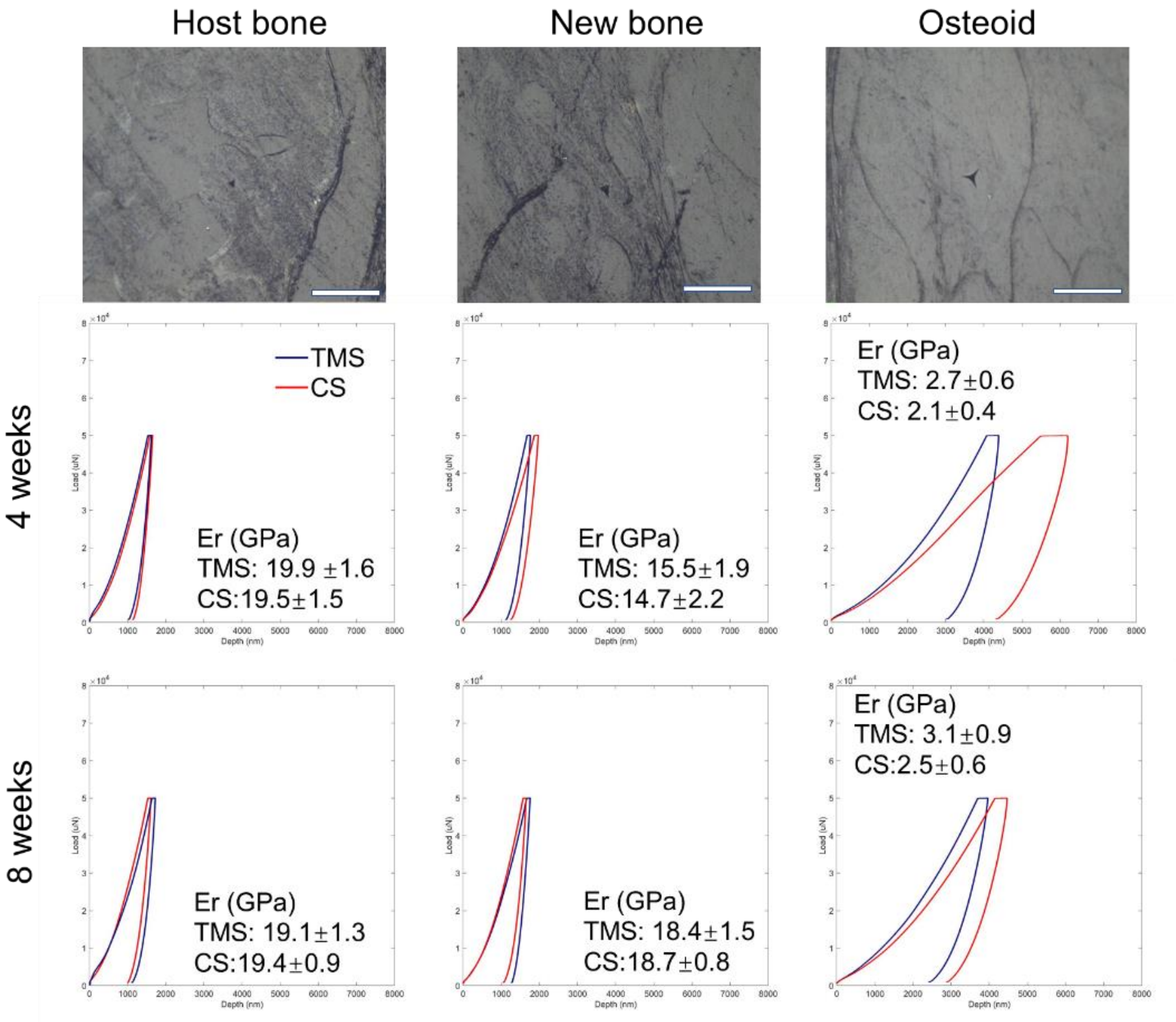

Fig. S14 Reduced modulus of bone tissues via nanoindentation tests. Indents were made in host bone, new bone and osteoid area of every specimen at each time. The elastic behavior was verified by observing the load–displacement curves. Data are presented as mean ± SD (n=5). Scale bars = 90 μm.

Supplementary Note 9: Protein sequencing and genetic data

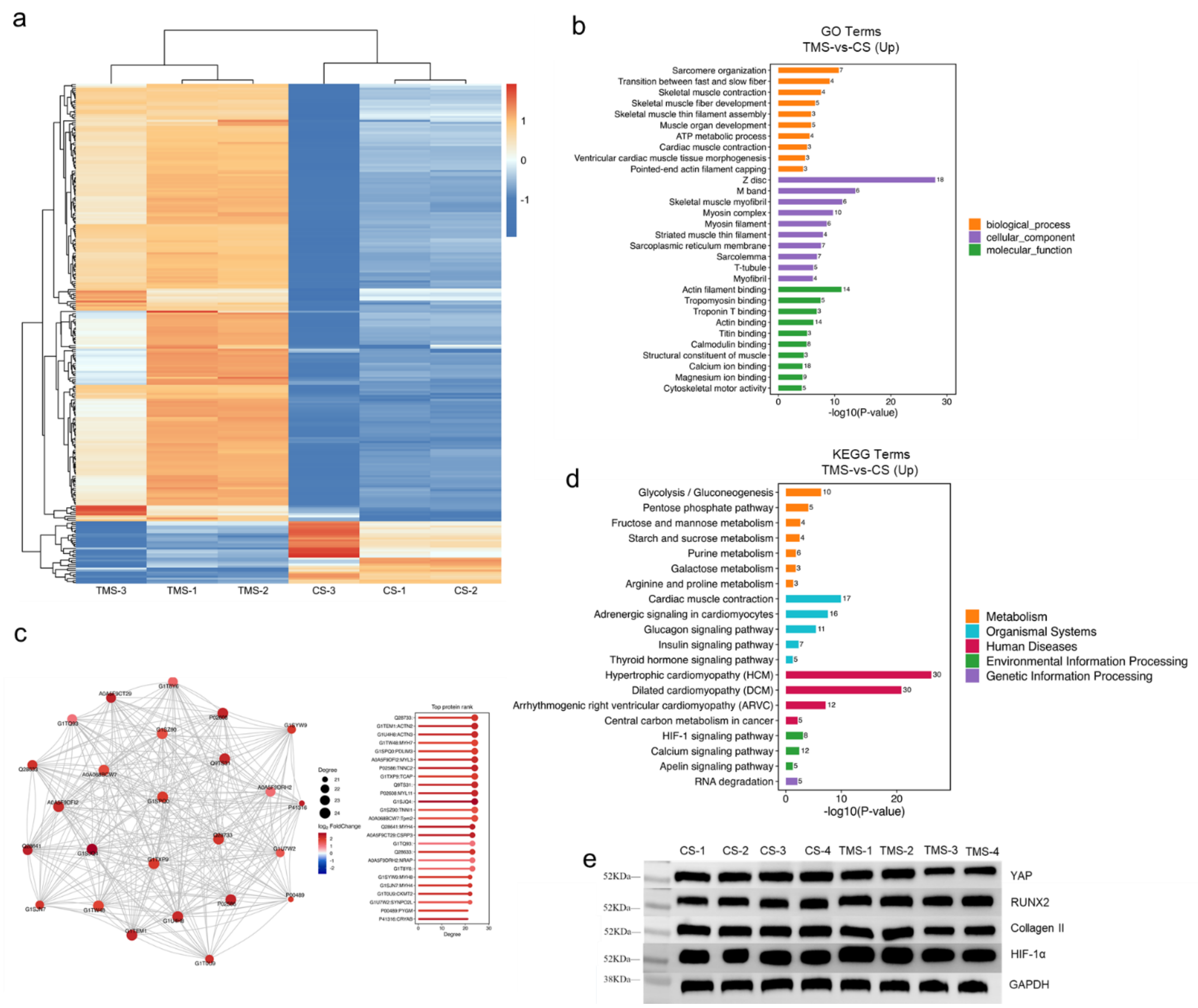

Fig. S15 Macroscopic proteomic results. **a** Different expression TMS-vs-CS heatmap shows 216 and 31 proteins were significantly up- and down-regulated. **b** Top 30 GO terms with respect to biological process, cellular component and molecular function. **c** Top25 Protein-protein interaction diagram, circles indicate differential proteins/genes, red represents up-regulation, green represents down-regulation, the size of the circle represents connectivity. **d** Top 20 KEGG terms. Besides bone regeneration related proteins, GO and KEGG terms suggest an upregulated of skeletal muscle and cellular force-sensing correlations. **e** Protein levels measured with Western blot (n=4).

Supplementary Note 10: Strain of cancellous bone inside scaffolds

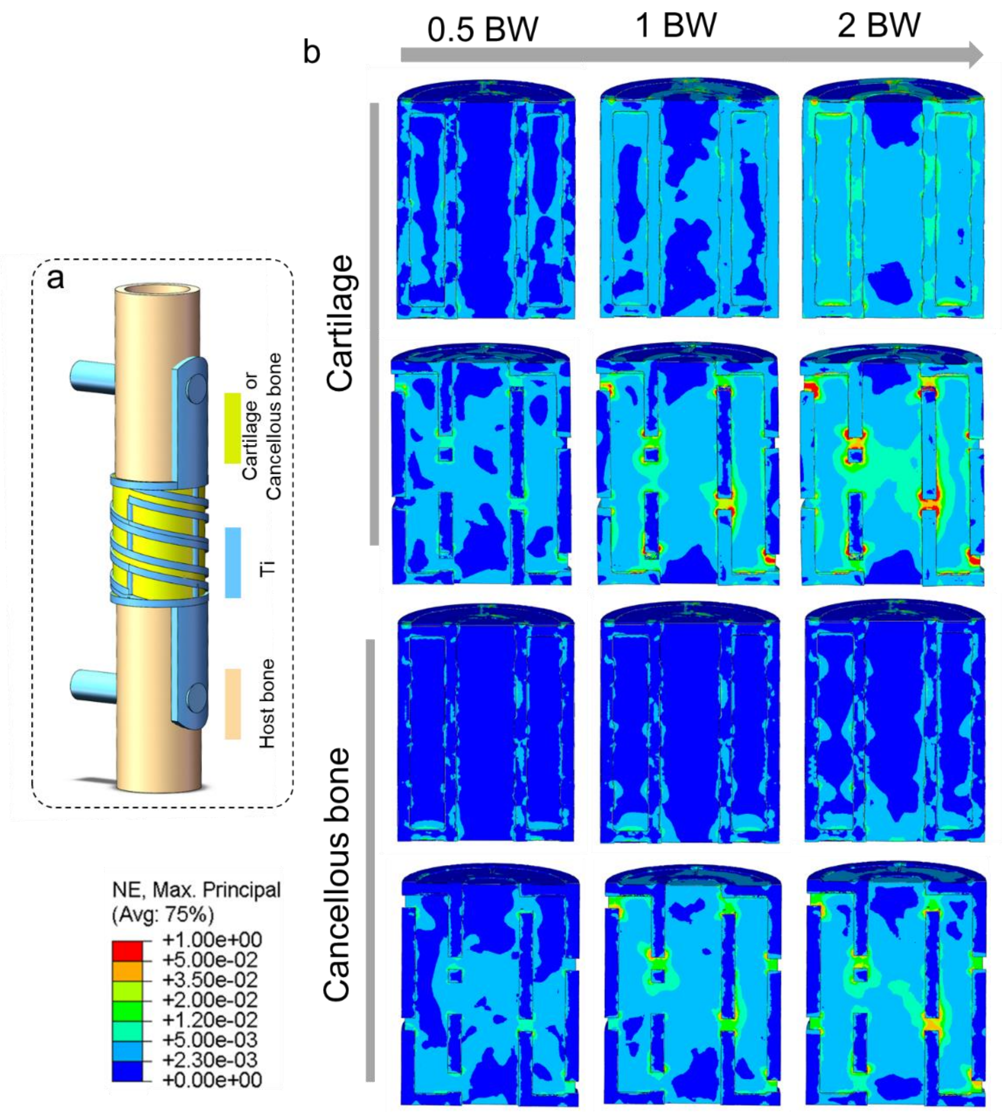

Fig. S16 FEM of the defect after cartilage or cancellous bone regeneration under different loads. a Illustration of implanted TMS with bone tissue. **b, c** Maximum principal strains of CS and TMS within the cartilage or cancellous bone and scaffolds under different the body weight

Supplementary Note 11: Compression simulation accuracy

As shown in Fig. S16 and Fig. 2d, the simulated modulus for the first stage is 14.3 MPa, while the experimental value is 13.4 ± 2.2 MPa. For the second stage, the simulated modulus is 338 MPa, compared to the experimental value of 318 ± 30 MPa. The primary discrepancy between the simulation and experimental results lies in the inflection point strain, which is larger in the simulation. This difference arises because, as illustrated in Fig. S1, the additively manufactured samples have rougher and more uneven surfaces compared to the designed surfaces, resulting in an actual l_g that is smaller than the design value.

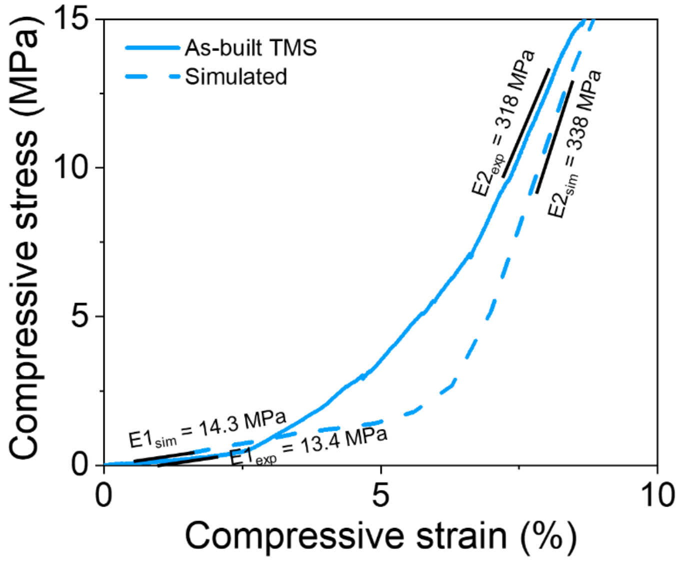

Fig. S17 The simulated strain-stress curves of TMS compared with experiments. The simulated curve is plotted with dash line, while experimental curve is plotted with solid line.

Supplementary Reference

[1] L. Yang, C. Yan, W. Cao, et al., Compression–compression fatigue behaviour of gyroid-type triply periodic minimal surface porous structures fabricated by selective laser melting, Acta Materialia 181 (2019) 49-66.